

Mermaid Cereal: Interactions and Pattern Formation in a Macroscopic Magnetocapillary SALR System

Alireza Hooshanginejad,¹ Jack-William Barotta,¹ Victoria Spradlin,^{1,2}

Giuseppe Pucci,^{3,4} Robert Hunt,¹ and Daniel M. Harris^{1,*}

¹*Center for Fluid Mechanics, School of Engineering,
Brown University, Providence, RI, US.*

²*The Wheeler School, Providence, RI, US.*

³*Consiglio Nazionale delle Ricerche - Istituto di Nanotecnologia (CNR-NANOTEC),
Via P. Bucci 33C, 87036 Rende, Italy*

⁴*Université Rennes, CNRS, IPR (Institut de Physique
de Rennes) UMR 6251, FR35000 Rennes, France*

(Dated: March 5, 2024)

Abstract

When particles are deposited at a fluid interface they tend to aggregate by capillary attraction to minimize the overall potential energy of the system. In this work, we embed floating millimetric disks with permanent magnets to introduce a competing repulsion effect and study their pattern formation in equilibrium. The pairwise energy landscape of two disks is described by a short-range attraction and long-range repulsion (SALR) interaction potential, previously documented in a number of microscopic systems. Such competing interactions enable a variety of pairwise equilibrium states, including the possibility of a local minimum energy corresponding to a finite disk spacing. Two-dimensional (2D) experiments and simulations in confined geometries demonstrate that as the areal packing fraction is increased, the dilute repulsion-dominated lattice state becomes unstable to the spontaneous formation of localized clusters, which eventually merge into a system-spanning striped pattern. Finally, we demonstrate that the equilibrium pattern can be externally manipulated by the application of a supplemental vertical magnetic force that remotely enhances the effective capillary attraction.

* daniel_harris3@brown.edu

INTRODUCTION

Self-assembly is the spontaneous formation of organized structures or patterns that are governed by interactions between the individual constituents of a system [1]. Methods for controlling self-assembly at the microscale often focus on tuning the interactions between the constituents of the system through internal [2–4] or external means [5–7]. Mathematically their interactions can be described by a pair interaction potential, which represents the work required to bring a pair of isolated particles from infinite separation to a finite distance apart [8]. In many cases, interaction potentials are composed of competing attractive and repulsive forces, with their relative strength and extent defining the possible structures achievable in the self-assembly of soft materials [9]. One class of competing interactions are defined by short-range attraction and long-range repulsion (SALR) forces, and have been documented for proteins in low-salinity solutions [10–12] and charged or magnetic colloidal particles in suspension [13–15], among others. SALR interaction potentials are sometimes referred to as *mermaid* potentials due to the “attractive head” and “repulsive tail” constituting their energy landscape [16]. Overall, laboratory investigations of SALR systems are typically reserved to the microscale. In the present work, we realize a complementary *macroscopic* 2D SALR system that can be used to probe the fundamentals of equilibrium self-assembly in an accessible tabletop platform.

In general, short-range attraction favors particle clustering while long-range repulsion inhibits gelation [17–19], and large systems of particles often arrange into liquid-like states composed of finite equilibrium clusters [18, 20, 21]. The patterns observed for such microscopic systems of particles primarily depend on the particle packing fraction and system temperature [21–23]. Regardless of the physical origin of such competing forces in a system of SALR particles, different structures can be predicted using models that apply techniques such as molecular dynamics [24–26] or Monte Carlo methods [27, 28].

While commonly used to characterize interactions at the microscale, pairwise interaction potentials are relevant at all scales – for instance, the interaction of celestial bodies can be described by a pairwise gravitational potential. Of relevance to the present study, two bodies resting at a mutual fluid interface can be described by an interaction potential considering the gravitational and surface energy of the system. Identical axisymmetric particles tend to attract one another to minimize the total energy anomaly introduced by

their presence, an effect often referred to as capillary attraction [29] or the ‘‘Cheerios effect’’ [30]. This phenomenon has been theoretically rationalized in various studies [29–36], and experimentally measured at both the microscopic [37–39] and macroscopic scales [40, 41]. Capillary attraction between floating objects is a fundamental problem with relevance to applications involving self-assembly at fluid interfaces in natural systems [42–45] and laboratory settings [46–48]. To prevent complete particle aggregation under capillary attraction, prior works have introduced repulsive magnetic dipole-dipole interactions through the application of an external magnetic field [49–52]. However, previous work at the macroscale has predominantly focused on short-range effects, with limited attention to the consequences of the relative long-range nature of the magnetic repulsion [50]. Furthermore, the region of approximately uniform magnetic field in the Helmholtz coil geometry used in the prior experiments sets practical limits on the number of particles and the size of the domain that can be considered.

In this work, floating millimetric disks are embedded with permanent magnetic dipoles giving rise to a tunable SALR interaction potential. We isolate the possible pairwise equilibrium states in this macroscopic magnetocapillary SALR system through a combination of experiment and mathematical modeling, with the full landscape captured by two non-dimensional parameters. After establishing the pairwise interaction landscape, we investigate the pattern formation of our magnetocapillary disks experimentally and numerically under varying packing fractions. We finally demonstrate external control of the self-assembly process in our magnetocapillary system by adjusting the capillary attraction strength remotely.

RESULTS

We systematically investigate the pairwise energy potential defined by capillary attraction and magnetic repulsion. We cast millimetric silicone-based hydrophobic disks of radius a and mass m , and embed each with a vertically polarized cylindrical magnet of magnetic moment M in its center. We gently deposit a magnetocapillary disk on the surface of a water-glycerol mixture followed by a second disk with distance l from the first disk as shown in Fig. 1(a). A complete description of the fabrication process for the magnetocapillary disks and fluid details are provided in the Methods section. Because the disks are hydrophobic,

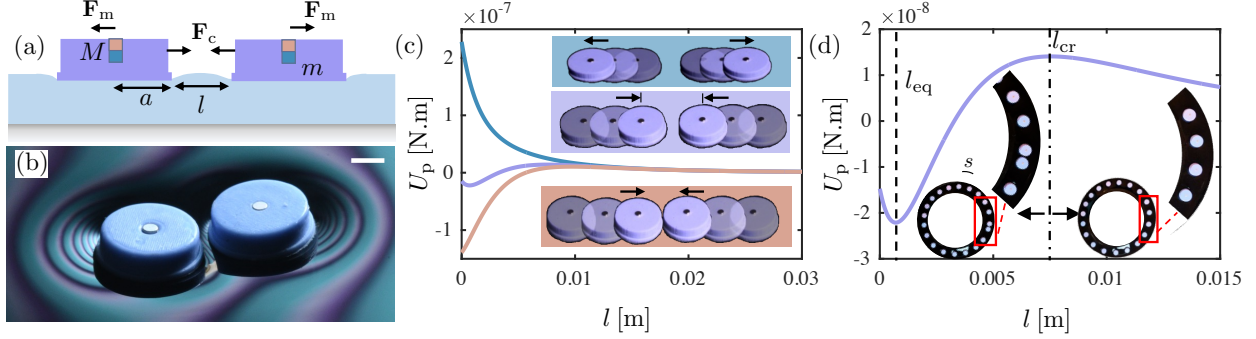


FIG. 1. **Experimental setup and regimes of the magnetocapillary interaction potential.**

(a) Schematics of two magnetocapillary disks of radius a and mass m each embedded with a small permanent magnet of magnetic dipole M . (b) In certain parameters regimes, two magnetocapillary disks find an equilibrium state defined by a finite spacing. The scale bar indicates 2 mm. (c) Sample magnetocapillary pairwise interaction potentials U_p versus interdisk spacing l . The three characteristic regimes are shown here (corresponding to the sequel snapshots in the inset): the locally attractive or Cheerios (red) regime, the mermaid (violet) regime, and the fully repulsive (blue) regime. For all three cases $a = 3$ mm and $M = 9$ A \cdot cm 2 with increasing masses of $m_1 = 0.080$ g, $m_2 = 0.092$ g, and $m_3 = 0.11$ g, respectively. Note that if the disks are started sufficiently far apart, they will always repel, as the magnetic repulsion decays at a slower rate than the capillary attraction. (d) Interaction potential for the sample mermaid regime. Inset: experiment shows that when the mean spacing in an annular 1D array drops below l_{cr} , disks begin to spontaneously pair.

each disk rests in equilibrium on the fluid surface under capillary flotation [53] with the contact line pinned along the sharp bottom edge. In the absence of magnetic effects, two disks are fully attracted to each other under the Cheerios effect [30]. Although an exact analytical formula is not available for the capillary attraction force between finite disks, it has been shown through experiments, simulation, and scaling that the capillary attraction force between them can be well approximated by a decaying exponential of the form [41]

$$\mathbf{F}_c = -F_0 e^{-l/\ell_c} \hat{e}_l. \quad (1)$$

Here, \hat{e}_l denotes the unit vector in the radial direction away from the adjacent disk, and $\ell_c = \sqrt{\gamma/\rho_m g}$ denotes the capillary length where γ and ρ_m denote water-glycerol surface tension and density, respectively. ℓ_c takes a fixed value of 2.4 mm for our experiments

corresponding to the choice of working fluid. F_0 is the characteristic attractive force found to be $2(mg)^2 a^{1/2} / \left(\pi^2 \gamma \ell_c^{3/2} [(a/\ell_c)^2 + 2a/\ell_c]^2 \right)$ for circular disks at the capillary scale (i.e. $a \gtrsim \ell_c$) [41]. The exponential form is reminiscent of the shape of a 2D meniscus determined by the linearized Young-Laplace equation [54]. Since the magnet size is negligible compared to the disk center-to-center spacing ($2a + l$), the magnets can be considered point dipoles with the repulsive magnetic force approximated as

$$\mathbf{F}_m = \frac{3\mu_0 M^2}{4\pi(l+2a)^4} \hat{e}_l, \quad (2)$$

where μ_0 denotes the permeability of free space [55]. The total pairwise interaction force is denoted by $\mathbf{F}_p = \mathbf{F}_m + \mathbf{F}_c$. Defining U_m as the magnetic energy potential, and U_c as the capillary energy potential where $\mathbf{F}_m = -\nabla U_m$ and $\mathbf{F}_c = -\nabla U_c$, the magnetocapillary interaction can also be expressed as an interaction potential $U_p = U_m + U_c$, defined as

$$U_p = \frac{\mu_0 M^2}{4\pi(l+2a)^3} - F_0 \ell_c e^{-l/\ell_c}. \quad (3)$$

As evident in Eq. (3), $|\mathbf{F}_m|$ decays algebraically with l while $|\mathbf{F}_c|$ decays exponentially. Depending on the input parameters, \mathbf{F}_p can have 0, 1, or 2 roots (equilibria) for the physically relevant regime $l \geq 0$. As a result, three characteristically different interaction regimes emerge. If $\mathbf{F}_p(l=0) < 0$ (i.e. locally attractive), then there is only 1 root, and it represents an unstable equilibrium at l_{cr} where the interaction switches from attractive to repulsive, and is a consequence of the different decay properties of the two functions. Hence, the disks either repel each other for $l > l_{cr}$, or collapse into each other for $l < l_{cr}$. We refer to this regime as the *Cheerios* regime, since it features the local (complete) collapse behavior characteristic of the Cheerios effect [30]. Figure 1(c) shows U_p as a function of l for a sample Cheerios regime with the solid red line.

If $\mathbf{F}_p(l=0) > 0$ (i.e. locally repulsive), \mathbf{F}_p can have either 0, or 2 roots for $l > 0$. The former is referred to as the *fully repulsive* regime, and an example is represented by the solid blue line in Fig. 1(c). When \mathbf{F}_p has 2 roots, the first root, l_{eq} , is a stable equilibrium point, while the second root, l_{cr} , is an unstable equilibrium point with example as the purple solid lines in Figs. 1(c) and 1(d). Under such a scenario, l_{eq} represents a potential well, where the two disks will reach equilibrium at a finite spacing as shown experimentally in Figs. 1(b) and 1(c) inset. We refer to this regime as the *mermaid* regime since it presents a SALR system most reminiscent of the SALR systems previously realized at the colloidal scale [16].

Note that the Cheerios regime also formally represents a SALR regime, but the presence of static friction due to the possibility of physical contact between the disks renders exploration of pattern formation less predictable and reproducible. In the mermaid regime, a pair of disks repel each other if they are positioned $l > l_{\text{cr}}$ apart, but fall into $l = l_{\text{eq}}$ if $l < l_{\text{cr}}$. The experimental realizations shown in Figure 1(c) show that for a single disk size and magnetic strength, the three regimes can be accessed by gradually increasing the disk mass, therein increasing the strength of the capillary attraction alone, effectively moving from the fully repulsive to mermaid to Cheerios regimes.

Figure 1(d) inset images show a segment of a 1D array of magnetocapillary mermaid disks confined in an annular channel of width 15 mm with the corresponding pairwise energy potential presented in Fig. 1(d). Under low packing fractions, the disks are all positioned above the l_{cr} threshold, securely in the repulsive tail of the energy potential. Given the channel's central radius, R , and the number of magnetocapillary mermaid disks, N , the mean distance between the disks, s , can be estimated as $(2\pi R - 2Na)/N$. For the magnetocapillary mermaid regime demonstrated in Fig. 1(d), $l_{\text{cr}} = 7.5$ mm. As shown in Fig. 1(d) inset, when $R = 6$ cm and $a = 6$ mm, for $N = 19$ the disks are spaced uniformly with anticipated $s = 7.8$ mm. However, by adding one more disk to the channel (i.e. $N = 20$), the anticipated spacing under uniform distribution is 6.8 mm, now lower than l_{cr} . Under this scenario, the new disk pairs up with the closest disk at the equilibrium spacing position (Fig. 1(d) inset), breaking the symmetry of the original 1D crystalline pattern.

We fabricated disks with different radius (a), mass (m), and magnetic moment (M) to more exhaustively verify our magnetocapillary potential model, and identify the limits of the various interaction regimes. To facilitate this exploration, we first normalize \mathbf{F}_p by the characteristic capillary force F_0 , and the disk spacing l by the disk diameter $2a$. Hence, we arrive at a nondimensional interaction force

$$F_p^* = \mathcal{M}(l^* + 1)^{-4} - e^{-2\sqrt{\text{Bo}}l^*}, \quad (4)$$

where the asterisks denote the nondimensionalized force and spacings. Two non-dimensional parameters emerge that govern the interaction: the gravitational Bond number $\text{Bo} = (a/\ell_c)^2$ that represents the strength of gravity to capillary forces, and a magnetocapillary number $\mathcal{M} = 3\mu_0 M^2 / 64\pi a^4 F_0$ that represents the ratio between the magnetic and capillary forces, in a similar spirit to prior work [50] but adapted to our larger length scales.

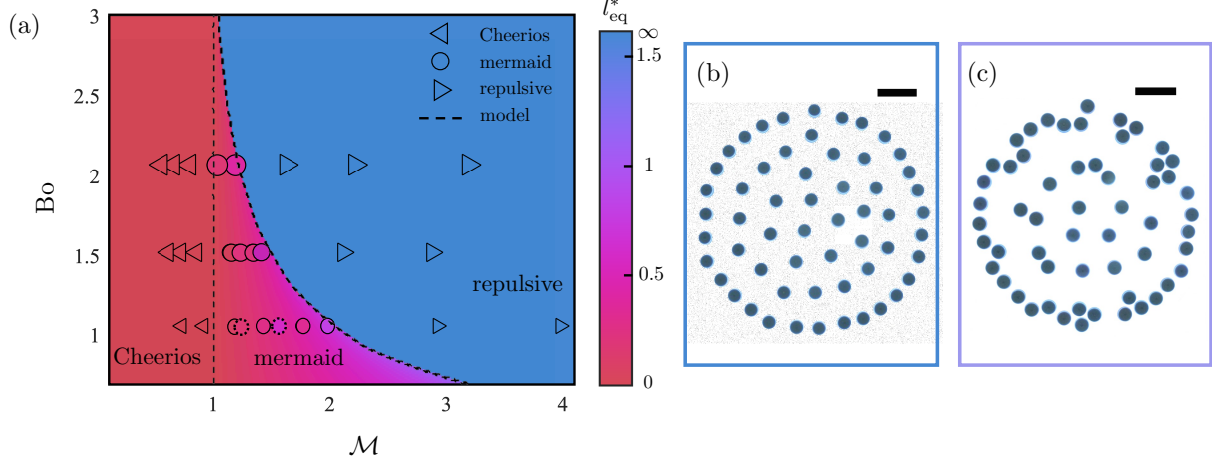


FIG. 2. **Magnetocapillary interactions.** (a) The phase diagram for different regimes as a function of capillary Bond number Bo and magnetocapillary number \mathcal{M} . The left triangles (\triangleleft) show the Cheerios regime, the right triangles (\triangleright) show the repulsive regime, and the circles (\circ) show the mermaid regime, as observed in the experiments. The symbol sizes correspond to three disk sizes, $a = 2.5$ mm, $a = 3$ mm, and $a = 3.5$ mm, hence three different Bo in ascending order. The phase diagram is color coded based on l_{eq}^* computed from the model, while the circles are color coded based on l_{eq}^* value measured in the experiments. The symbols with solid outlines represent magnets with $M = 9$ A \cdot cm 2 while the dashed-line outlined symbols represent disks with permanent magnets of $M = 2.25$ A \cdot cm 2 . While Bo is only varied by a in our experiments, \mathcal{M} is varied with a , m , and M . The dashed lines indicate the model prediction for boundaries between different regimes. The dimensional parameters and equilibrium spacing for each experiment is provided in the supplemental material. (b) The equilibrium configuration in experiment for fully repulsive disks with $\mathcal{M} = 2.1$, $Bo = 1.52$, and $\phi = 0.1425$ ($a = 3$ mm, $m = 0.073$ g, $M = 9$ A \cdot cm $^{-2}$, $R = 6$ cm, $N = 57$). (c) The equilibrium configuration in the experiments for mermaid disks with $\mathcal{M} = 1.22$, $Bo = 1.52$, and $\phi = 0.1425$ ($a = 3$ mm, $m = 0.092$ g, $M = 9$ A \cdot cm $^{-2}$, $R = 6$ cm, $N = 57$).

We find the roots of F_p^* for $l^* > 0$ and varying Bo and \mathcal{M} . For $Bo \leq 4$ three possible states exist, which we delineate by the number of roots satisfying $l^* > 0$. The transition between 0 roots to 2 roots marks the boundary between the fully repulsive regime and the mermaid regime, and is demarcated by the curve $\mathcal{M} = \frac{16}{Bo^2} e^{-2\sqrt{Bo}-4}$. The transition from 2 roots to 1 root marks the boundary between the mermaid and Cheerios regimes and is

demarcated by $\mathcal{M} = 1$. These predictions are summarized in Figure 2(a) by the dashed lines, showing that the mermaid regime is only possible in a finite range of parameter space. The color spectrum indicates the predicted equilibrium spacing distance l_{eq}^* (when finite). At $\text{Bo} = 4$, $\mathcal{M} = 1$, a triple point is predicted to exist between the three phases, and above $\text{Bo} \geq 4$ the mermaid regime is predicted to vanish entirely. For $\text{Bo} \geq 4$, only the Cheerios and fully repulsive regimes exist, switching over at $\mathcal{M} = 1$.

The root corresponding to the inevitable transition to long-range repulsion (l_{cr}^*) can be found analytically, and is given by

$$l_{\text{cr}}^* = -\frac{2}{\sqrt{\text{Bo}}} \mathcal{W}_{-1}(\Theta(\mathcal{M}, \text{Bo})) - 1. \quad (5)$$

Here, \mathcal{W}_k represents the k -th branch of the Lambert \mathcal{W} function, and its argument $\Theta(\mathcal{M}, \text{Bo}) = -\frac{2\mathcal{M}^{1/4}}{\sqrt{\text{Bo}}} e^{-\sqrt{\text{Bo}}/2}$. As described above, l_{cr}^* is a positive finite value in both the Cheerios and mermaid regimes. Furthermore, the second root (l_{eq}^*) can be expressed as

$$l_{\text{eq}}^* = -\frac{2}{\sqrt{\text{Bo}}} \mathcal{W}_0(\Theta(\mathcal{M}, \text{Bo})) - 1, \quad (6)$$

and takes a finite positive value only in the mermaid regime. For $\mathcal{M} < 1$ (i.e. in the Cheerios regime) the value of (l_{cr}^*) becomes negative, corresponding to a physically inaccessible equilibrium location inside the disk. Steric contact forces between the disks thus balance the residual local attraction in this regime, with the disks in solid contact with one another. More details regarding exact solutions for the equilibrium points and phase boundaries can be found in the supplementary material.

The overlaid points on Figure 2(a) show the experimentally observed interaction regime under different combinations of parameters. The experimental points in the mermaid regime are similarly color coded by their measured equilibrium spacing. Complete details of the parameters associated with each experimental symbol are presented in the supplemental material. The model prediction for both the extent of the mermaid regime and the measured l_{eq} value are in very good agreement with the experimental data, validating the accuracy of our magnetocapillary SALR interaction model. Further quantitative comparison of l_{eq} for the controlled parameters is provided in the supplemental material.

We perform 2D experiments to investigate how the pairwise interactions in magnetocapillary disks scale up in larger collections under the various regimes presented in Fig. 2(a). A circular confinement corral is filled with a water-glycerol mixture, and has a 1.5 cm opening

connected to a smaller bath where the disks are deposited and individually directed toward the main confinement. The pattern is allowed to stabilize before the next disk is introduced. The confinement corral is slightly underfilled, so the border meniscus acts as a non-steric repulsive barrier. We control the magnetocapillary disks areal packing fraction $\phi = Na^2/R^2$, where N denotes the number of disks in a circular 2D confinement, and $R = 6$ cm denotes the confinement radius. In the absence of magnets, the disks collapse into a single granular raft under unimpeded capillary attraction [56]. As shown in Fig. 2(b), fully repulsive disks with $a = 3$ mm, $m = 0.073$ g, and $M = 9$ A·cm⁻² ($\mathcal{M} = 2.1$ and $\text{Bo} = 1.52$) exhibit a hexagonal crystal lattice at $\phi = 0.1425$. However, as shown in Fig. 2(c) mermaid disks of the same size and same magnet dipole strength with slightly higher mass at $m = 0.092$ g ($\mathcal{M} = 1.22$ and $\text{Bo} = 1.52$) form clusters at $\phi = 0.1425$. Due to confinement effects, disks first begin pairing along the boundary. We use the pairwise interaction potential provided in Eq. 3 to perform an N -body simulation on a confined 2D system of N magnetocapillary disks. In addition, a localized confining potential models the boundary of the fluid container. The overdamped equation of motion for each disk i is

$$\frac{\mu(\pi a^2)}{H} \dot{\mathbf{x}}_i = \mathbf{F}_{\text{confining},i} + \sum_{j \neq i} (\mathbf{F}_{c,ij} + \mathbf{F}_{m,ij}), \quad (7)$$

where \mathbf{x}_i denotes the position vector for disk i with respect to the center of the circular confinement, the dot represents the derivative with respect to time, and H and μ are the liquid bath depth and viscosity, respectively. The confining force, $\mathbf{F}_{\text{confining}} = -\nabla U_{\text{confining}}$, is assumed to be governed by a confining potential of form $U_{\text{confining}}(r) = \frac{\alpha}{2} \left[1 + \tanh \left(\frac{r+a-R}{\ell_c} \right) \right]$. Although the exact functional form is not important here, the form used is chosen to provide a repulsive barrier that decays away from the system boundary over the capillary length scale, capturing the influence of the repulsive meniscus barrier in a fluid container. Here, r denotes the radial distance from the disks center to the center of the circular confinement, R denotes the confinement radius, and α is a constant corresponding to the depth of the potential well tuned to be sufficiently large to prevent particles from escaping the corral. The initial positions of the disks are sampled from a uniform distribution with resampling occurring in the case of disk-disk overlap. The positions of all disks are then evolved in time as $2N$ first-order ODEs according to Eq. 7. The `ode45` solver in MATLAB is used to iterate the system of ordinary differential equations. The underdamped version of Eq. 7

(i.e. $4N$ equations) gives indistinguishable results for the equilibrium state, justifying the overdamped simplification for our particular exploration.

To further study the equilibrium pattern formation of the magnetocapillary disks in the mermaid regime, we perform 2D experiments and simulations under different areal packing fractions ϕ . As shown in Fig. 3(a) top row for $a \ll R$, the system exhibits a hexagonal lattice state at $\phi = 0.05$. As we increase ϕ in 0.05 increments, the magnetocapillary mermaid disks begin pairing spontaneously, with clusters forming at $\phi = 0.1$ and 0.15. At $\phi = 0.2$ the system shows stripe patterns until transitioning to labyrinths at $\phi = 0.25$. Figure 3(a) bottom row shows the simulation results under confinement for the same physical parameters as in the experiments while varying ϕ , with good agreement. To explore any influence of geometrical confinement on the pattern formation (a practical necessity in experiment), simulations are also completed with periodic boundary conditions in a large square domain (17 cm \times 17 cm) that is 2.5 times larger than the confinement area in the experiments. As shown in Fig. 3(b), similar patterns and transitions arise, albeit with more spatial homogeneity due to the absence of a true border.

To quantitatively characterize the simulated patterns in 2D, we construct a radial distribution function (RDF) [57]. The RDF for disk i , $g_i(r)$, is given by $g_i(r) = K_{i,[r,r+\Delta r]}/(2\pi r\Delta r)$ where $K_{i,[r,r+\Delta r]}$ denotes the number of disks located at a distance of r to $r + \Delta r$ from disk i . We can then obtain the average RDF for the entire system as $g(r) = \frac{1}{N} \sum_i^N g_i(r)$. To characterize the system's phase under the mermaid potential, we average $g(r)$ over 25 independent simulations for each ϕ in a square domain of 17 cm \times 17 cm with periodic boundary conditions. Figure 3(c) shows the average RDF $\bar{g}(r)$ as a function of the distance from the disks normalized by the equilibrium distance between two isolated disks, namely $\bar{l} = (l + 2a)/(l_{\text{eq}} + 2a)$. As indicated in Fig. 3(c), $\bar{g}(r)$ is small at $\phi = 0.05$ for $\bar{l} < 2$, with a maximum at $\bar{l} \approx 3.1$ which is the characteristic spacing in the hexagonal lattice formation for this packing fraction. For $\phi = 0.1$, the strongest peak emerges at $\bar{l} \approx 1$ indicative of the magnetocapillary mermaid stable equilibrium state and the appearance of clustering. With increasing ϕ , the clusters coalesce into longer chains of disks, hence, more peaks appear at integer multiples of $\bar{l} \approx 1$. The stripe and labyrinth phase exhibit similar RDFs [57]. These phases undergo a topological transition and could potentially be distinguished by alternative metrics, such as the corresponding Betti numbers or average pore size.

We further aim to showcase the tunability of our macroscopic system by manipulating the

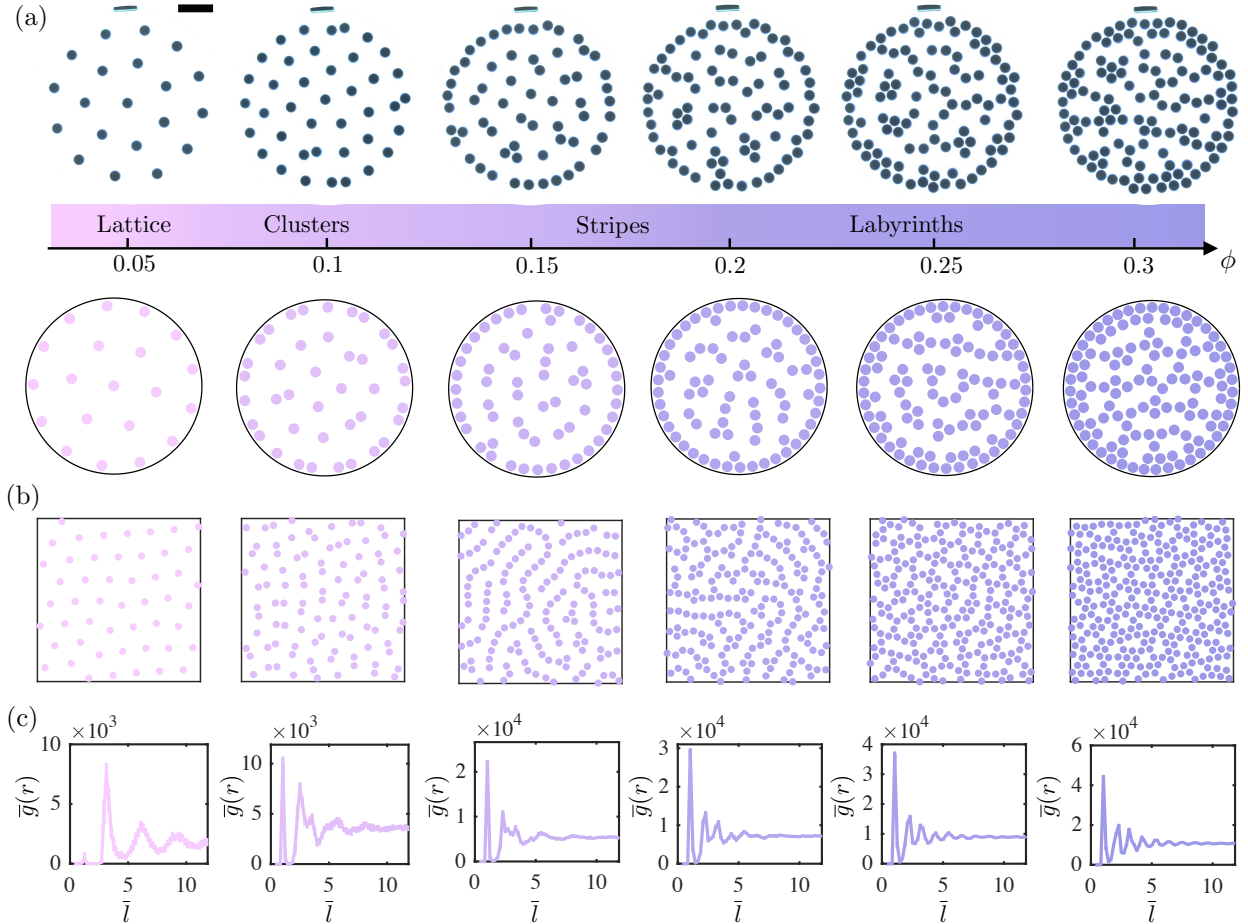


FIG. 3. **2D pattern formation in the magnetocapillary mermaid regime.** (a) Patterns formed by magnetocapillary mermaid disks with $\mathcal{M} = 1.22$ and $\text{Bo} = 1.52$ ($a = 3$ mm, $M = 9$ A $\cdot\text{cm}^{-2}$, $m = 0.092$ g) for varying areal packing fraction, ϕ . The confinement radius R is 6 cm. The top row illustrates the experimental snapshots starting from the hexagonal lattice state to clusters, stripes, and labyrinths. The bottom row shows sample model results color coded based on corresponding ϕ values in the experiments. (b) Simulation results of mermaid disks with the same parameters as (a) in a large square domain of 17 cm \times 17 cm with a periodic boundary condition for varying packing fraction, ϕ . (c) The average radial distribution function RDF, $\bar{g}(r)$, from the periodic boundary condition simulations in a square domain of 17 cm \times 17 cm as a function of \bar{l} averaged over 25 independent simulations for varying ϕ . The error bars indicate one standard deviation of the simulation results.

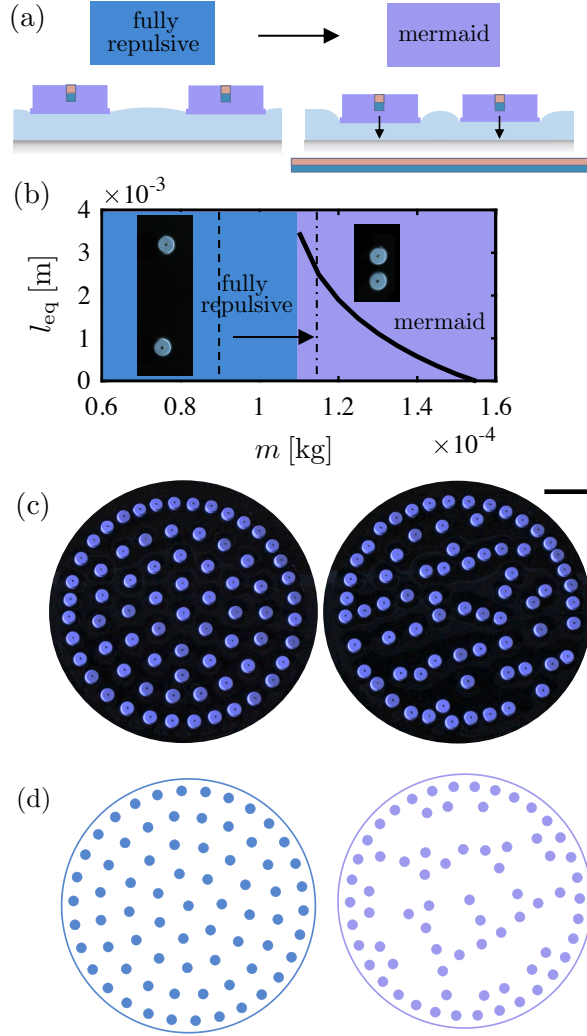


FIG. 4. **External control of equilibrium pattern.** (a) When a magnetic strip is placed below the bath, the disks are pulled downwards, increasing the capillary attraction force. If tuned correctly, fully repulsive disks can transition to mermaid disks under this additional force. (b) l_{eq} as a function of m from the magnetocapillary model for $a = 2.5$ mm, and $M = 9$ A·cm². The dashed-line shows the physical value of m while the dotted dashed-line shows the effective m after applying the external magnetic force based on the l_{eq} value extracted from the experiments shown in the inset. (c) The hexagonal lattice state (on the left) transitions to the striped pattern (right) by adding the magnetic strip below the bath for disks with $a = 2.5$ mm, $M = 9$ A·cm², and $m = 0.09$ g ($\text{Bo} = 1.05$, $\mathcal{M}=3.5$) and $\phi = 0.18$. The scale bar indicates 2 cm. (d) Sample magnetocapillary simulations for $a = 2.5$ mm, and $M = 9$ A·cm² showing phase transition from hexagonal lattice to stripes when m changes from 0.09 g to 0.115 g ($\text{Bo} = 1.05$ with \mathcal{M} decreasing from 3.5 to 1.9) for $\phi = 0.18$.

system phase remotely. We place a large magnetic sheet below the bath approximately 7 mm below the free surface as depicted in Fig. 4(a). A pair of magnetocapillary disks with $a = 2.5$ mm, $m = 0.09$ g, and $M = 9$ A·cm² ($B_0=1.05$, $\mathcal{M}=3.5$) show fully repulsive behavior as shown in Fig. 4(b) inset. However, as we place the magnetic strip below the bath, the disks are pulled down by the applied vertical magnetic force between the embedded magnets and the magnetic sheet resulting in a larger depression of the meniscus surrounding the disks, and hence a larger capillary force between the disks as illustrated in Fig. 4(a). This force increase is such that the fully repulsive disks in Fig. 4(b) transition to the mermaid regime and fall into the potential well configuration.

In the absence of a detailed characterization of the magnetic sheet, the increase in the capillary force is modeled by replacing the mass of the disk with an effective (greater) mass that yields the equilibrium spacing experimentally measured in a two-disk experiment under the additional uniform vertical magnetic force. From the experimental l_{eq} under the magnetic strip, we find the effective mass that yields the same l_{eq} using the model. Figure 4(b) shows the model solution with the solid line for l_{eq} versus m for $a = 2.5$ mm, and $M = 9$ A·cm². The dashed line shows the disks original mass (0.09 g), and the dotted dashed line shows the effective mass (0.115 g) corresponding to $l_{\text{eq}} = 2.6$ mm from the experimental inset. Therefore, we can model the system before and after adding the external magnetic strip by changing m from 0.09 g to 0.115 g in the magnetocapillary potential. Figures 4(c) and 4(d) show a 2D system of fully repulsive disks with the same disk parameters from experiments and simulations, respectively, for $\phi = 0.18$. The disks form a hexagonal lattice away from the boundary until the external magnetic strip is placed beneath, upon which the system immediately transitions to a stripe state. A video of this process is included with the supplementary material. As shown in Figs. 4(c) and 4(d), the simulation results with the effective mass is in good qualitative agreement with the experiments.

CONCLUSION

In summary, we have demonstrated that the competing interactions between the attractive capillary force and the repulsive magnetic force can result in a macroscopic SALR potential with rich self-assembly phenomenology reminiscent of colloidal SALR suspensions [58–61]. We have developed a magnetocapillary potential model defined by two non-dimensional

parameters that rationalizes the pairwise interaction between the magnetocapillary disks, and reproduces different phases of pattern formation for varying packing fractions. In addition, we have showed that by manipulating the capillary force, we can control the patterns externally. The current magnetocapillary SALR system provides an accessible playground for investigating analogous aspects of colloidal SALR systems where experiments are more challenging or expensive, and could also be used in pedagogy when introducing modern topics in self-assembly. To further establish connections with colloidal-scale SALR systems, future studies will explore simulating the effect of thermal fluctuations and Brownian motion via the addition of supercritical chaotic Faraday waves [62, 63].

METHODS

The disks were fabricated using OOMOO 30 which is a silicone rubber compound comprised of part A and part B that should be mixed 1:1 in volume or 10:13 in weight, respectively [64]. The density of the mixed compound under this scenario was $1.34 \pm 0.02 \text{ g}\cdot\text{cc}^{-1}$. We mixed 30 milliliters of part A and 30 milliliters of part B for 30 seconds by hand with a wooden craft stick. We then poured the compound into a 3D-printed mold that was printed using a Formlabs Form 2 resin printer. After pouring the compound into the mold, the mold was placed in a small vacuum chamber and degassed for 5 minutes to extract air bubbles trapped inside the mold. Next, we scraped the surface of the mold using a blade to make a smooth and balanced surface on the mold. The compound cured inside the mold for at least 6 hours in room temperature. We then used a compressed air nozzle to remove the disks from the mold.

In order to robustly achieve a smooth and axisymmetric three-phase contact line when depositing disks, we designed the molds with a thin lip around the disks edge that was 0.25 mm high and 0.25 mm thick. We also cast a cylindrical recession in the center of the disk for placing magnets. We used Neodymium 50 magnets (Supermagnetman) of 1 mm height and two different diameters of 0.5 mm and 1 mm (corresponding to $M = 2.25 \text{ A}\cdot\text{cm}^2$ and $M = 9 \text{ A}\cdot\text{cm}^2$, respectively). To place a magnet inside a disk, we used the south pole of a permanent magnet underneath the disks to get a magnet inside the hole. We then removed the permanent magnet while manually holding the installed magnet in the disk.

For the working fluid, we used a mixture of water-glycerol with density, $\rho_m = 1139.0 \pm 0.3$

$\text{kg}\cdot\text{m}^{-3}$, measured with a density meter (Anton Paar DMA 35A), surface tension, $\gamma = 0.068 \pm 0.001 \text{ N}\cdot\text{m}^{-1}$, and dynamic viscosity, $\mu = 0.0083 \pm 0.0004 \text{ N}\cdot\text{s}\cdot\text{m}^{-2}$ [65]. The fluid is gently poured into a circular confinement corral made from laser-cut acrylic sheets of thickness 6 mm to a depth of $H = 5$ mm.

ACKNOWLEDGEMENTS

The authors would like to acknowledge Ryan Poling-Skutvik for fruitful discussions. A.H. acknowledges the Hibbitt Fellowship. J.-W.B. is supported by the Department of Defense through the National Defense Science and Engineering Graduate (NDSEG) Fellowship Program. G.P. acknowledges the CNR-STM and the CNRS-Momentum Programs. This work is partially supported by the Office of Naval Research (ONR N00014-21-1-2816).

AUTHOR CONTRIBUTIONS

A.H., J.-W.B., G.P., and D.M.H. designed research, analyzed data, developed models, and wrote the paper; A.H. and V.S. performed final experiments; A.H. and R.H. analyzed the models; J.-W.B. developed and performed simulations; all authors performed research, discussed the results, commented on the manuscript and gave final approval for publication, agreeing to each be held accountable for the work performed therein; D.M.H. supervised the project and secured funding.

COMPETING INTERESTS

The authors declare no competing interests.

ADDITIONAL INFORMATION

Supplementary information 1 supplementary document and 5 supplementary videos available. All code and data associated with the numerical simulations can be found at

<https://github.com/harrislab-brown/MermaidCereal>.

- [1] G.M. Whitesides and B. Grzybowski, “Self-assembly at all scales,” *Science* **295**, 2418–2421 (2002).
- [2] M.R. Caplan, P.N. Moore, S. Zhang, R.D. Kamm, and D.A. Lauffenburger, “Self-assembly of a β -sheet protein governed by relief of electrostatic repulsion relative to van der waals attraction,” *Biomacromolecules* **1**, 627–631 (2000).
- [3] Q. Li, Y. Jia, L. Dai, Y. Yang, and J. Li, “Controlled rod nanostructured assembly of diphenylalanine and their optical waveguide properties,” *ACS Nano* **9**, 2689–2695 (2015).
- [4] M.A. Elsaywy, A.M. Smith, N. Hodson, A. Squires, A.F. Miller, and A. Saiani, “Modification of β -sheet forming peptide hydrophobic face: Effect on self-assembly and gelation,” *Langmuir* **32**, 4917–4923 (2016).
- [5] Gang Wei, Jörg Reichert, and Klaus D Jandt, “Controlled self-assembly and templated metallization of fibrinogen nanofibrils,” *Chemical communications* , 3903–3905 (2008).
- [6] A.C. Dave, S.M. Loveday, S.G. Anema, G.B. Jameson, and H. Singh, “Modulating beta-lactoglobulin nanofibril self-assembly at pH 2 using glycerol and sorbitol,” *Biomacromolecules* **15**, 95–103 (2014).
- [7] R. Li, C.C. Horgan, B. Long, A.L. Rodriguez, L. Mather, C.J. Barrow, D.R. Nisbet, and R.J. Williams, “Tuning the mechanical and morphological properties of self-assembled peptide hydrogels via control over the gelation mechanism through regulation of ionic strength and the rate of pH change,” *RSC Advances* **5**, 301–307 (2015).
- [8] Erle C. Donaldson and Waqi Alam, “Chapter 1 - wettability,” in *Wettability*, edited by Erle C. Donaldson and Waqi Alam (Gulf Publishing Company, 2008) pp. 1–55.
- [9] M. Engel and H.R. Trebin, “Self-assembly of monatomic complex crystals and quasicrystals with a double-well interaction potential,” *Physical Review Letters* **98**, 225505– (2007).
- [10] A. Tardieu, S. Finet, and F. Bonneté, “Structure of the macromolecular solutions that generate crystals,” *Journal of Crystal Growth* **232**, 1–9 (2001).
- [11] R. Piazza, “Protein interactions and association: an open challenge for colloid science,” *Current Opinion in Colloid & Interface Science* **8**, 515–522 (2004).

- [12] M.C. Abramo, C. Caccamo, D. Costa, G. Pellicane, R. Ruberto, and U. Wanderlingh, “Effective interactions in lysozyme aqueous solutions: A small-angle neutron scattering and computer simulation study,” *The Journal of Chemical Physics* **136**, 035103 (2012).
- [13] J. Wu, D. Bratko, and J.M. Prausnitz, “Interaction between like-charged colloidal spheres in electrolyte solutions,” *Proceedings of the National Academy of Sciences* **95**, 15169–15172 (1998).
- [14] Y. Liu and Y. Xi, “Colloidal systems with a short-range attraction and long-range repulsion: Phase diagrams, structures, and dynamics,” *Current Opinion in Colloid & Interface Science* **39**, 123–136 (2019).
- [15] A. Al Harraq, A.A. Hymel, E. Lin, T.M. Truskett, and B. Bharti, “Dual nature of magnetic nanoparticle dispersions enables control over short-range attraction and long-range repulsion interactions,” *Communications Chemistry* **5**, 72 (2022).
- [16] C.P. Royall, “Hunting mermaids in real space: known knowns, known unknowns and unknown unknowns,” *Soft Matter* **14**, 4020–4028 (2018).
- [17] F. Sciortino, S. Mossa, E. Zaccarelli, and P. Tartaglia, “Equilibrium cluster phases and low-density arrested disordered states: The role of short-range attraction and long-range repulsion,” *Physical Review Letters* **93**, 055701– (2004).
- [18] A.I. Campbell, V.J. Anderson, J.S. van Duijneveldt, and P. Bartlett, “Dynamical arrest in attractive colloids: The effect of long-range repulsion,” *Physical Review Letters* **94**, 208301– (2005).
- [19] E. Zaccarelli, “Colloidal gels: equilibrium and non-equilibrium routes,” *Journal of Physics: Condensed Matter* **19**, 323101 (2007).
- [20] A. Stradner, H. Sedgwick, F. Cardinaux, W.C.K. Poon, S.U. Egelhaaf, and P. Schurtenberger, “Equilibrium cluster formation in concentrated protein solutions and colloids,” *Nature* **432**, 492–495 (2004).
- [21] P. Douglas Godfrin, Néstor E. Valadez-Pérez, Ramon Castañeda-Priego, Norman J. Wagner, and Yun Liu, “Generalized phase behavior of cluster formation in colloidal dispersions with competing interactions,” *Soft Matter* **10**, 5061–5071 (2014).
- [22] P.N. Pusey and W. van Megen, “Phase behaviour of concentrated suspensions of nearly hard colloidal spheres,” *Nature* **320**, 340–342 (1986).

- [23] J. Pękalski, E. Bildanau, and A. Ciach, “Self-assembly of spiral patterns in confined systems with competing interactions,” *Soft Matter* **15**, 7715–7721 (2019).
- [24] C. Reichhardt, C.J. Olson Reichhardt, I. Martin, and A. R. Bishop, “Dynamical ordering of driven stripe phases in quenched disorder,” *Physical Review Letters* **90**, 026401– (2003).
- [25] C.J. Olson Reichhardt, C. Reichhardt, I. Martin, and A.R. Bishop, “Dynamics and melting of stripes, crystals, and bubbles with quenched disorder,” *Physica D: Nonlinear Phenomena* **193**, 303–309 (2004).
- [26] Y.H. Liu, L.Y. Chew, and M.Y. Yu, “Self-assembly of complex structures in a two-dimensional system with competing interaction forces,” *Physical Review E* **78**, 066405– (2008).
- [27] E. Dickinson and R. Euston, “Monte carlo simulation of colloidal systems,” *Advances in Colloid and Interface Science* **42**, 89–148 (1992).
- [28] B.V.R. Tata and N. Ise, “Monte carlo study of structural ordering in charged colloids using a long-range attractive interaction,” *Physical Review E* **58**, 2237–2246 (1998).
- [29] W. A. Gifford and L. E. Scriven, “On the attraction of floating particles,” *Chemical Engineering Science* **26**, 287–297 (1971).
- [30] D. Vella and L. Mahadevan, “The “Cheerios effect”,” *American Journal of Physics* **73**, 817–825 (2005).
- [31] D.Y.C. Chan, J.D. Henry, and L.R. White, “The interaction of colloidal particles collected at fluid interfaces,” *Journal of Colloid and Interface Science* **79**, 410–418 (1981).
- [32] P.A. Kralchevsky, V.N. Paunov, I.B. Ivanov, and K. Nagayama, “Capillary meniscus interaction between colloidal particles attached to a liquid—fluid interface,” *Journal of Colloid and Interface Science* **151**, 79–94 (1992).
- [33] M.M. Müller, M. Deserno, and J. Guven, “Geometry of surface-mediated interactions,” *Europhysics Letters* **69**, 482 (2005).
- [34] J-B. Fournier, “On the stress and torque tensors in fluid membranes,” *Soft Matter* **3**, 883–888 (2007).
- [35] A. Domínguez, M. Oettel, and S. Dietrich, “Force balance of particles trapped at fluid interfaces,” *The Journal of Chemical Physics* **128**, 114904 (2008).
- [36] A. He, K. Nguyen, and S. Mandre, “Capillary interactions between nearby interfacial objects,” *Europhysics Letters* **102**, 38001 (2013).

- [37] R. Di Leonardo, F. Saglimbeni, and G. Ruocco, “Very-long-range nature of capillary interactions in liquid films,” *Physical Review Letters* **100**, 106103– (2008).
- [38] B.J. Park and E.M. Furst, “Attractive interactions between colloids at the oil–water interface,” *Soft Matter* **7**, 7676–7682 (2011).
- [39] V. Carrasco-Fadanelli and R. Castillo, “Measurement of the force between uncharged colloidal particles trapped at a flat air/water interface,” *Soft Matter* **15**, 5815–5818 (2019).
- [40] J.M. Rieser, P.E. Arratia, A.G. Yodh, J.P. Gollub, and D.J. Durian, “Tunable capillary-induced attraction between vertical cylinders,” *Langmuir* **31**, 2421–2429 (2015).
- [41] I. Ho, G. Pucci, and D.M. Harris, “Direct measurement of capillary attraction between floating disks,” *Physical Review Letters* **123**, 254502– (2019).
- [42] D.L. Hu and J.W.M. Bush, “Meniscus-climbing insects,” *Nature* **437**, 733–736 (2005).
- [43] J.W.M. Bush, D.L. Hu, and M. Prakash, “The integument of water-walking arthropods: Form and function,” in *Advances in Insect Physiology*, Vol. 34, edited by J. Casas and S.J. Simpson (Academic Press, 2007) pp. 117–192.
- [44] J. Voise, M. Schindler, J. Casas, and E. Raphaël, “Capillary-based static self-assembly in higher organisms,” *Journal of The Royal Society Interface* **8**, 1357–1366 (2011).
- [45] P. Peruzzo, A. Defina, H.M. Nepf, and R. Stocker, “Capillary interception of floating particles by surface-piercing vegetation,” *Physical Review Letters* **111**, 164501– (2013).
- [46] N. Bowden, A. Terfort, J. Carbeck, and G.M. Whitesides, “Self-assembly of mesoscale objects into ordered two-dimensional arrays,” *Science* **276**, 233–235 (1997).
- [47] I.B. Liu, N. Sharifi-Mood, and K.J. Stebe, “Capillary assembly of colloids: Interactions on planar and curved interfaces,” *Annual Review of Condensed Matter Physics* **9**, 283–305 (2018).
- [48] C. Zeng, M.W. Faaborg, A. Sherif, M.J. Falk, R. Hajian, M. Xiao, K. Hartig, Y. Bar-Sinai, M.P. Brenner, and V.N. Manoharan, “3d-printed machines that manipulate microscopic objects using capillary forces,” *Nature* , 1–6 (2022).
- [49] M. Golosovsky, Y. Saado, and D. Davidov, “Energy and symmetry of self-assembled two-dimensional dipole clusters in magnetic confinement,” *Physical Review E* **65**, 061405– (2002).
- [50] N. Vandewalle, L. Clermont, D. Terwagne, S. Dorbolo, E. Mersch, and G. Lumay, “Symmetry breaking in a few-body system with magnetocapillary interactions,” *Physical Review E* **85**, 041402– (2012).

- [51] G. Grosjean, M. Hubert, and N. Vandewalle, “Magnetocapillary self-assemblies: Locomotion and micromanipulation along a liquid interface,” *Advances in Colloid and Interface Science* **255**, 84–93 (2018).
- [52] G. Lagubeau, G. Grosjean, A. Darras, G. Lumay, M. Hubert, and N. Vandewalle, “Statics and dynamics of magnetocapillary bonds,” *Physical Review E* **93**, 053117– (2016).
- [53] D. Vella, D. Lee, and H. Kim, “The load supported by small floating objects,” *Langmuir* **22**, 5979–5981 (2006).
- [54] Pierre-Gilles Gennes, Françoise Brochard-Wyart, David Quéré, et al., *Capillarity and wetting phenomena: drops, bubbles, pearls, waves* (Springer, 2004).
- [55] A. Abragam, *The Principles of Nuclear Magnetism*, International series of monographs on physics (Clarendon Press, 1961).
- [56] S. Protière, C. Josserand, J. M. Aristoff, H. A. Stone, and M. Abkarian, “Sinking a granular raft,” *Phys. Rev. Lett.* **118**, 108001 (2017).
- [57] H.J. Zhao, V.R. Misko, and F.M. Peeters, “Analysis of pattern formation in systems with competing range interactions,” *New Journal of Physics* **14**, 063032 (2012).
- [58] H.M. McConnell, “Theory of hexagonal and stripe phases in monolayers,” *Proceedings of the National Academy of Sciences* **86**, 3452–3455 (1989).
- [59] M. Seul and D. Andelman, “Domain shapes and patterns: The phenomenology of modulated phases,” *Science* **267**, 476–483 (1995).
- [60] R. de Koker, W. Jiang, and H.M. McConnell, “Instabilities of the stripe phase in lipid monolayers,” *The Journal of Physical Chemistry* **99**, 6251–6257 (1995).
- [61] G. Malescio and G. Pellicane, “Stripe phases from isotropic repulsive interactions,” *Nature Materials* **2**, 97–100 (2003).
- [62] H. Xia, N. Francois, H. Punzmann, and M. Shats, “Tunable diffusion in wave-driven two-dimensional turbulence,” *Journal of Fluid Mechanics* **865**, 811–830 (2019).
- [63] S.J. Thomson, J-W. Barotta, and D.M. Harris, “Nonequilibrium capillary self-assembly,” (2023), arXiv:2309.01668 [cond-mat.soft].
- [64] J-W. Barotta, S.J. Thomson, L.F. L. Alventosa, M. Lewis, and D.M. Harris, “Bidirectional wave-propelled capillary spinners,” *Communications Physics* **6**, 87 (2023).
- [65] K. Takamura, H. Fischer, and N.R. Morrow, “Physical properties of aqueous glycerol solutions,” *Journal of Petroleum Science and Engineering* **98-99**, 50–60 (2012).